PAPER • **OPEN ACCESS**

Lasing in Zn-doped GaAs nanowires on an iron film

To cite this article: Gyanan Aman *et al* 2023 *Nanotechnology* **34** 445201

OPEN ACCESS
IOP Publishing
Nanotechnology
Nanotechnology **34** (2023) 445201 (8pp)
https://doi.org/10.1088/1361-6528/ace914

Lasing in Zn-doped GaAs nanowires on an iron film

Gyanan Aman[1], Mykhaylo Lysevych[2], Hark Hoe Tan[2], Chennupati Jagadish[2], Heidrun Schmitzer[3], Martin Fränzl[4], Marc Cahay[1] and Hans Peter Wagner[1,5]

[1] Department of Electrical and Computer Engineering, University of Cincinnati, Cincinnati, OH 45221, United States of America
[2] Department of Electronic Materials Engineering, ARC Center of Excellence for Transformative Meta-Optical Systems, Research School of Physics, The Australian National University, Canberra, ACT 2600, Australia
[3] Department of Physics, Xavier University, Cincinnati, OH 45207, United States of America
[4] Department of Physics, University of Leipzig, D-04109, Germany
[5] Department of Physics, University of Cincinnati, Cincinnati, OH 45221, United States of America

E-mail: wagnerhp@uc.edu

Received 11 April 2023, revised 23 June 2023
Accepted for publication 20 July 2023
Published 16 August 2023

Abstract

In this work, we demonstrate optically pumped lasing in highly Zn-doped GaAs nanowires (NWs) lying on an iron film. The conically shaped NWs are first covered with an 8 nm thick Al_2O_3 film to prevent atmospheric oxidation and mitigate band-bending effects. Multimode and single-mode lasing have been observed for NWs with a length greater or smaller than 2 μm, respectively. Finite difference time domain calculations reveal a weak electric field enhancement in the Al_2O_3 layer at the NW/iron film interface for the lasing modes. The high Zn acceptor concentration in the NWs provides enhanced radiative efficiency and enables lasing on the iron film despite plasmonic losses. Our results open avenues for integrating NW lasers on ferromagnetic substrates to achieve new functionalities, such as magnetic field-induced modulation.

Supplementary material for this article is available online

Keywords: hybrid photonic-plasmonic, nano-lasers, iron, single mode, magnetic modulation

(Some figures may appear in colour only in the online journal)

Introduction

Optical platforms based on photonic integrated circuits (PICs) can overcome the limitation of bandwidth, processing speed, and power consumption of microelectronics chips. This prospect has triggered the research on materials and designs that can manipulate light at the nanoscale and complement the functionalities of integrated circuits and devices such as transistors, amplifiers, and modulators [1–3]. Semiconductor nanowires (NWs), with their one-dimensional structure, high refractive index, and electromagnetic wave confinement at the nanoscale, are excellent candidates for optical platforms. They can operate as waveguides, lasers, modulators, phototransistors, and photodetectors, which are crucial elements in PICs [3–6]. Optical platforms with NW components will lead to advancements in applications such as telecommunication, sensing, and medical diagnostics [2, 7, 8].

An essential step towards integrating active and passive NW components in PICs is the controllability of their optical properties using an external agent. Different regulating mechanisms, such as voltage, temperature, and photons, have been used to achieve active photonic-plasmonic NW devices [9–11]. An alternative approach to control and manipulate

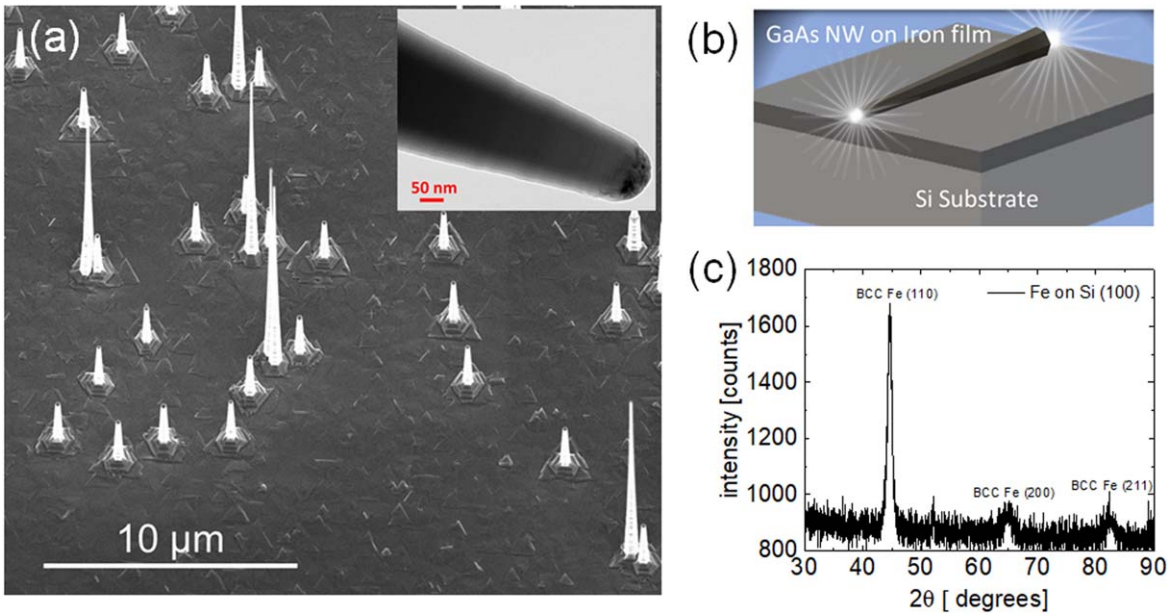

Figure 1. Structural characterization of NWs on Fe film: (a) SEM image of highly Zn-doped ($N_A = 2 \times 10^{19}$ cm^{-3}) GaAs NWs with a zincblende twinning superlattice structure. The length of the NWs ranged from 3.2 to 10 μm. The inset shows the TEM image of a Zn-doped GaAs NW coated with 8 nm of Al_2O_3 layer. (b) A schematic of the NW transferred on 400 nm thick iron film on Si substrate. (c) X-ray diffraction of the 400 nm iron film on Si (100) substrate.

their optical properties is with a magnetic field. A magnetic field with its ultrafast behavior is suitable for attaining a femtosecond level switching rate [12, 13]. An applied magnetic field on NW lasers could regulate photon generation [14] and carrier movement [15] inside NWs due to magneto-optic (MO) or magneto-plasmonic (MP) effects [16], similar to Faraday, Kerr, and Hall effects.

MO interaction in a photonic NW laser is constrained by the small Verdet constant of semiconductor materials [17]. Plasmonic NW lasers use Au and Ag as substrates which have moderate plasmonic losses but possess only meager MP properties. On the other hand, ferromagnetic materials exhibit strong magnetic field effects but have much higher plasmonic losses than noble metals, thereby limiting the possibility of MP waveguides and applications [12, 13].

This work demonstrates multimode and single mode lasing in hybrid photonic GaAs NWs on a plasmonic ferromagnetic Fe film. The NWs have a high Zn concentration of 2×10^{19} cm^{-3} and are covered with an 8 nm thick Al_2O_3 film to prevent oxidization and reduce band bending effects. The high acceptor concentration improves radiative recombination and decreases the transparency carrier density [18], thereby facilitating lasing despite plasmonic losses in the Fe film. The lasing experiments were theoretically supported by finite-difference time-domain (FDTD) simulations and light-output and light-input (*L–L*) calculations. The simulations demonstrate that the lasing modes have a weak plasmonic field enhancement within the Al_2O_3 interlayer between the NW and Fe film. The hybrid photonic-plasmonic nature of the modes leads to moderate plasmonic losses but has the potential to enhance magnetic field induced effects [19] due to the interaction of photogenerated carriers in the NW with the emerging magnetic fields from a magnetized iron substrate or its magnetic domains.

Our results using a ferromagnetic material like Fe as a substrate provide a path for adding new magnetic field induced functionalities to hybrid photonic-plasmonic NW lasers, isolators, modulators, and interconnects, similar to MP structures [19, 20] but with significantly reduced plasmonic losses.

Methods

Growth and characterization of the GaAs NWs and of the iron film

The NWs were produced by a gold catalyzed, metal-organic vapor phase epitaxy process [18, 21] under the same experimental condition and with the same Zn acceptor doping level of $N_A = 2 \times 10^{19}$ cm^{-3} as described in [18] and in the supplementary document (paragraph 1). Figure 1(a) shows the SEM image of the GaAs NWs grown on GaAs (111) substrate. These NWs have an average length of 3.2 μm with a few as long as 10 μm. The bright/dark contrast on the NWs indicate a twinning superlattice structure because of the effect of Zn doping [18]. The NWs were coated with an 8 nm thick Al_2O_3 by atomic layer deposition to minimize band bending effects (see TEM image in inset figure 1(a)).

For the experiments, the NWs were mechanically transferred with a small brush onto a ~400 nm thick Fe film (purity of 99.995%) deposited on a silicon (100) substrate through e-beam evaporation at a rate of 2–3 Å s^{-1} at room temperature. The transferred NWs break into random lengths varying from 1 to 6 μm and tip diameters varying from 150 to 400 nm. Figure 1(b) shows the schematic of a GaAs NW laser lying on

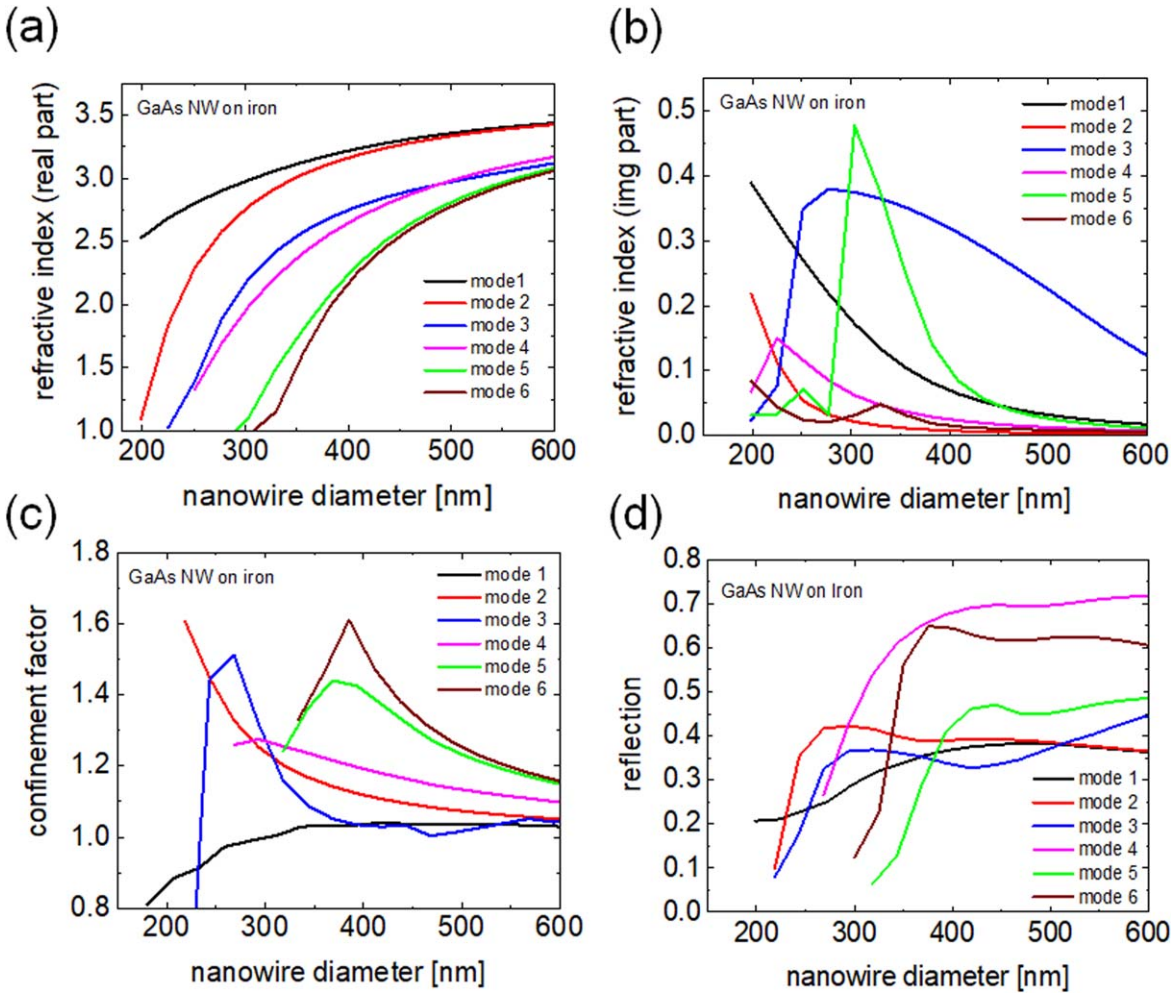

Figure 2. Optical parameters of the Al_2O_3/GaAs NW on iron film calculated for different NW diameters: (a) effective refractive index (real part), (b) imaginary part of the refractive index, (c) confinement factor of NW on iron film, and (d) facet reflection of GaAs NW.

the Fe/Si substrate. Figure 1(c) shows the x-ray diffraction spectrum of the Fe film on Si (100) substrate, recorded using the Kα Cu radiation of wavelength $\lambda = 1.54056$ Å, in the range of 30°–90°. The spectrum shows a prominent diffraction peak at 44.6° and two smaller peaks, 65° and 82°, corresponding to the Fe (110), Fe (200), and Fe (211) Bragg reflection of a body-centered crystal structure, respectively. The strong intensity of the (110) peak indicates that the orientation of the film is predominantly in ⟨110⟩ direction, which is expected for e-beam evaporated Fe film [22]. The lattice constant was calculated using Bragg's and Scherrer's formula to 2.87 Å, similar to the bulk lattice constant, and the width of the peaks revealed a Fe crystallite size of ∼9 nm, indicating a polycrystalline film. Atomic force microscopy (shown in figure S1(a) of the supplementary document) shows a root mean square surface roughness of 0.35 nm for the Fe film. The profilometry of the Fe film (an example of the measure is shown in figure S1(b) in the supplementary document) returned a thickness of 380 ± 20 nm. The NWs on the Fe film were further investigated by scanning electron microscopy (SEM) to obtain their accurate dimensions. The transfer of the NWs, together with the identification and characterization of the lasing properties of the NWs are described in [23].

FDTD calculations of GaAs NW on iron films

The optical parameters of GaAs NWs such as waveguide mode profiles, effective refractive indices (n_{eff}), group refractive indices n_g, plasmonic losses (α_p), absorption cross sections (σ_{abs}), reflectivity losses (α_R), and confinement factors (Γ) for six different modes were calculated using FDTD and Lumerical *Mode Solution* packages [23]. In the simulations, an un-tapered, hexagonal, and conical NW with a diameter of 200–600 nm surrounded with an 8 nm Al_2O_3 layer, lying on an iron film was modeled. The material parameters of silicon, Al_2O_3, GaAs, and iron film at the wavelength of 880 nm in the calculations were taken from the literature [24, 25]. To account for the variation of the effective refractive index and the κ value for its conical shape, the values are averaged using the functions $n_{\text{eff}} = \int_{d_t}^{d_b} n(d)\delta d/(d_b - d_t)$ and $\kappa_{\text{eff}} = \int_{d_t}^{d_b} \kappa(d)\delta d/(d_b - d_t)$ where d_t is the tip diameter, and d_b is the bottom diameter of the truncated NW under investigation.

Figure 2(a) shows the refractive index (real part) $n(d)$ for Al_2O_3/GaAs NW on iron film. A mode cut-off for the NW was considered when the refractive index values reached ∼1 (identical to air). The imaginary refractive index $\kappa(d)$ that

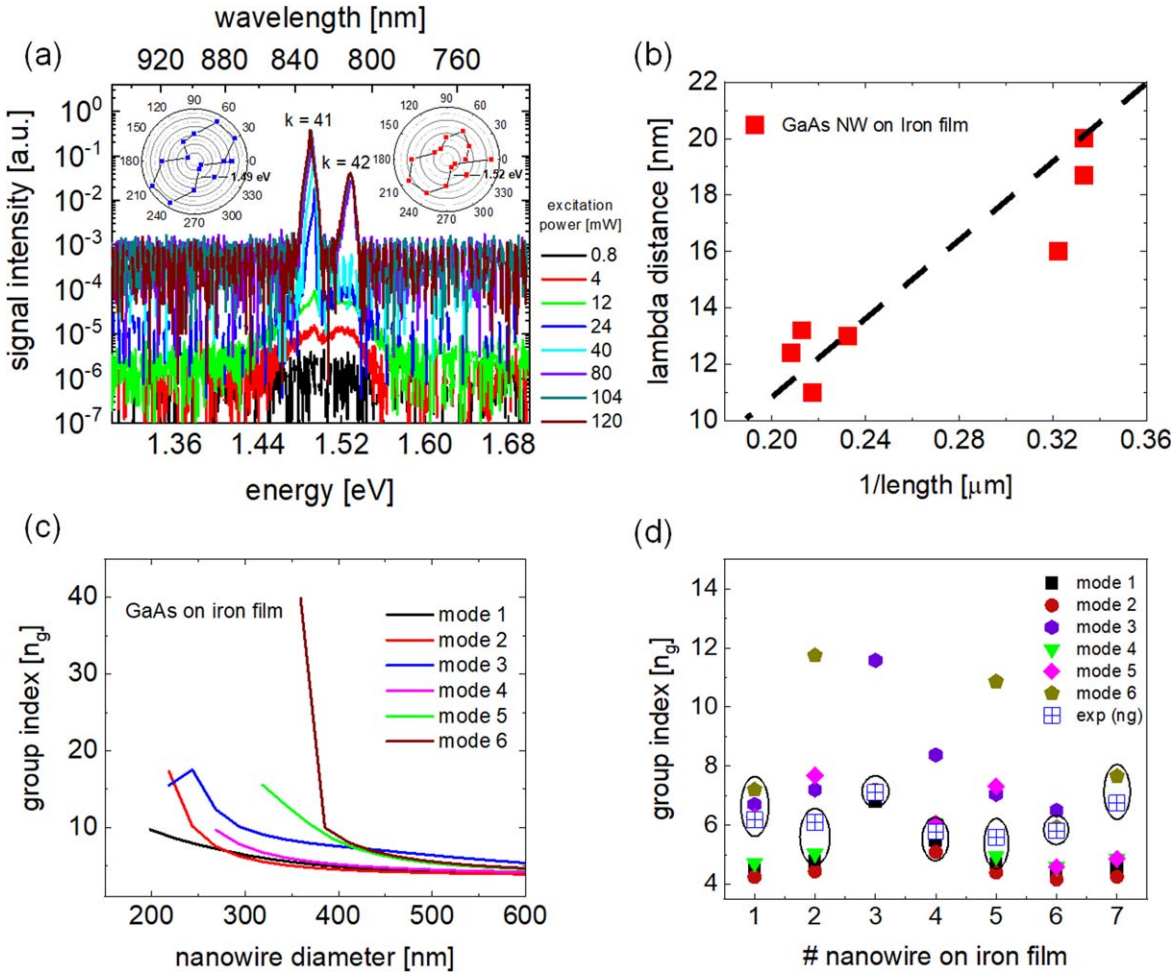

Figure 3. Lasing from GaAs NWs on iron film: (a) power dependent lasing measurements from a single NW at 77 K at an excitation wavelength of 720 nm. (b) Mode distance $\Delta\lambda$ of the longitudinal modes as a function of $1/L$ (length) of all investigated NWs. The dash line is a fitting to the experimental data (red squares). (c) Group index (n_g) of the 6 possible modes for NW diameters ranging from 200 to 600 nm on iron film, calculated using FDTD. (d) Comparison of the experimentally and theoretically calculated group indices and the designation of the supported transverse lasing mode in the NWs.

signifies the losses due to the iron film is shown in figure 2(b). The losses for mode 1 and mode 2 were highest for NWs with a diameter of 200 nm, which decrease with diameter. Mode 2 shows the lowest losses for NWs with a tip diameter greater than 300 nm. Mode 3 has high losses, which increase exponentially from a diameter of 200–300 nm and later decrease as the diameter approaches 600 nm. Like mode 3, mode 5 presents a similar trend in the variation of the imaginary refractive index with diameter, with highest losses for 300 nm diameter NWs. Modes 2 and 6 show an analogous trend as a function of the diameter and have the least losses for NWs with a diameter larger than 400 nm, indicating a pure photonic mode. The intermediate losses in modes 4 and 5 below a diameter of 400 nm suggest a hybrid photonic lasing with plasmonic confinement in the Al_2O_3 layer between the NW and the iron film. Modes 1 and 3 show high losses below 400 nm, indicating pure plasmonic modes.

The confinement factor of the 6 modes for the NW on the iron film is depicted in figure 2(c). Analogous to the effective index, the confinement factor was averaged considering the tip and base diameter. The confinement factor decreases suddenly for all the NWs near their cutoff. All modes show a confinement factor greater than 1 for diameters larger than 350 nm. The confinement factors of modes 2–6 decrease when the NWs reach a diameter of ∼600 nm. Mode 1 offers constant confinement of ∼1 for diameters greater than 350 nm. Mode 6 shows the highest confinement factor among all 6 modes and displays a value of ∼1.6 at a diameter of ∼400 nm. Mode 2 has the highest confinement factor of ∼1.6 at a cutoff diameter of 200 nm and decreases rapidly to ∼1 as the diameter increases to 600 nm. The facet reflection of the GaAs NWs on the iron film as a function of NW tip diameter is shown in figure 2(d). The reflectivity of the conical NWs was calculated by finding the geometric mean of R_t and R_b, calculated as $R = \sqrt{R_t R_b}$.

Results and discussion

Lasing experiments on GaAs NWs lying horizontally on a Fe film were performed in an optical setup described in [23]. The NW sample was placed inside a liquid nitrogen-cooled

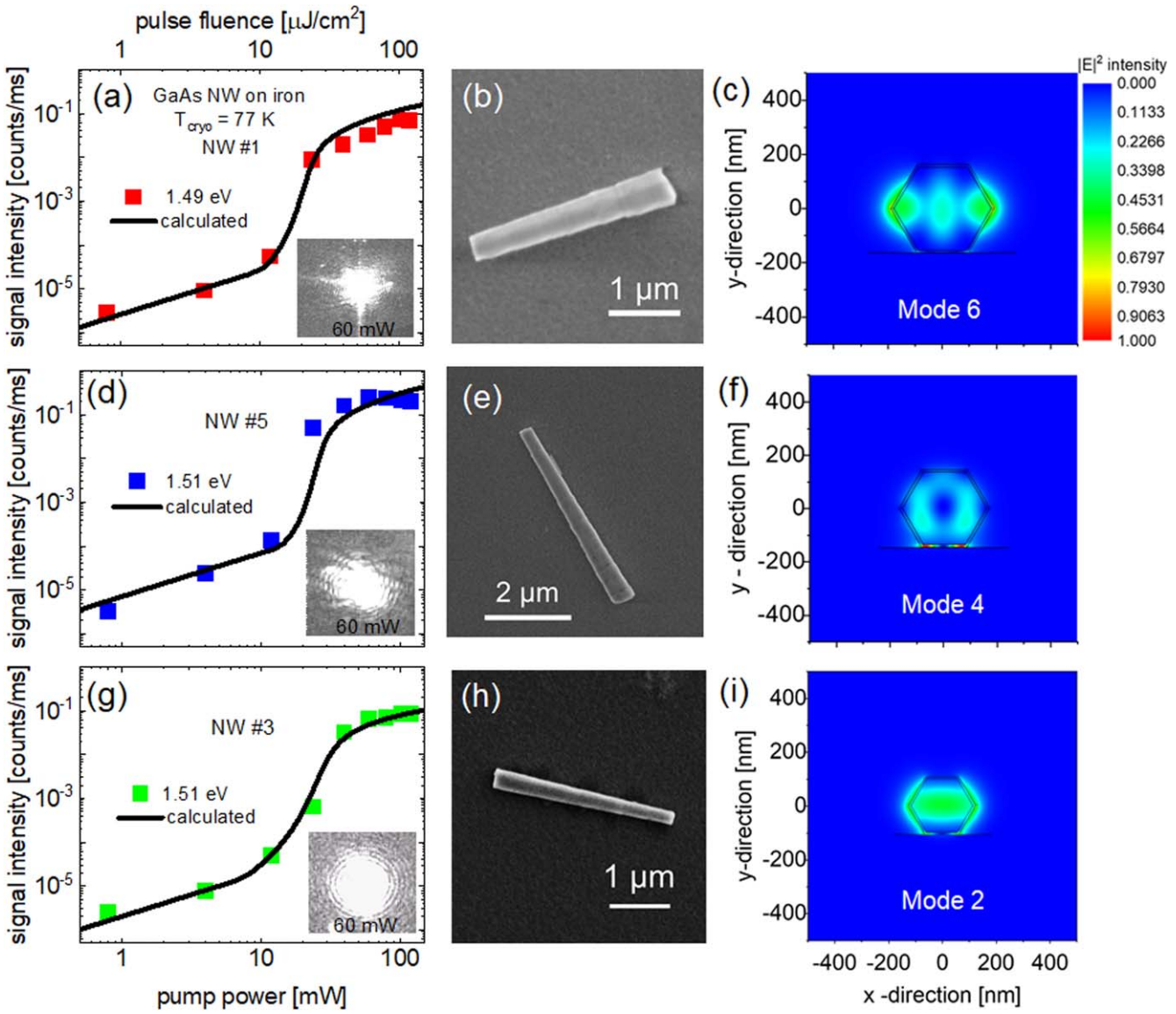

Figure 4. Peak intensity versus pump fluence (*L–L* plot) and lasing modes: figures (a), (d), and (g) show the *L–L* plots of NW #1, #5, #3. Figures (b), (e) and (h) show SEM images of NW #1, NW#5 and NW#3. Images (c), (f), and (i) depict the cross-sectional electric field profiles of the lasing modes of the corresponding NW.

cryostat, and single NWs were excited with ultrashort laser pulses tuned to a wavelength $\lambda_p = 720$ nm. The beam diameter on the sample was 40 μm. Excitation power dependent measurements were performed at a cryostat temperature $T_{\text{cryo}} = 77$ K. The emission from each NW was sent through a polarizer to analyze the lasing modes. Figure 3(a) shows the power dependent emission from a single NW on the Fe film. At a low pump power of 4 mW, the NW emits a broad photoluminescence spectrum. With increasing pump power to 12 mW, the broad spectrum becomes narrower. At a pump power of 40 mW, the emission intensity at 1.49 eV increases exponentially, indicating the onset of amplified spontaneous emission, which converts to lasing at higher pump levels because of the increasing optical gain. Increasing the pump power also extends the gain spectrum to higher energy (see figure S18(a) in [23]) leading to a second longitudinal laser mode with an energy position at 1.52 eV. Pump power levels above 80 mW narrow the emission linewidths to a few nanometers, signifying the onset of lasing of the second longitudinal mode. Polarization dependent measurements (displayed in the inset of figure 3(a)) indicate that the two longitudinal modes at 1.49 and 1.52 eV originate from the same NW. SEM (shown in figure 4(b)) revealed that the emission originates from a NW with a length of 3 μm, with a tip diameter (t_d) of 370 nm and a base diameter (b_d) of 580 nm. The mode distance $\Delta\lambda$ of the laser emission is ~20 nm. The expression $n_g = \lambda_L^2/2L\Delta\lambda_L$, where λ_L is the emission wavelength, provides a group index of $n_g = 5.72$. This index corresponds to the longitudinal mode numbers $k = 41$ and 42 for the 1.49 eV and 1.52 eV laser lines, respectively. Figure 3(b) shows the mode distance $\Delta\lambda$ versus the inverse NW length ($1/L$) of several NWs. The dimensions of these NWs and the resulting experimental group indices are summarized in table ST1 in the supplementary document. The

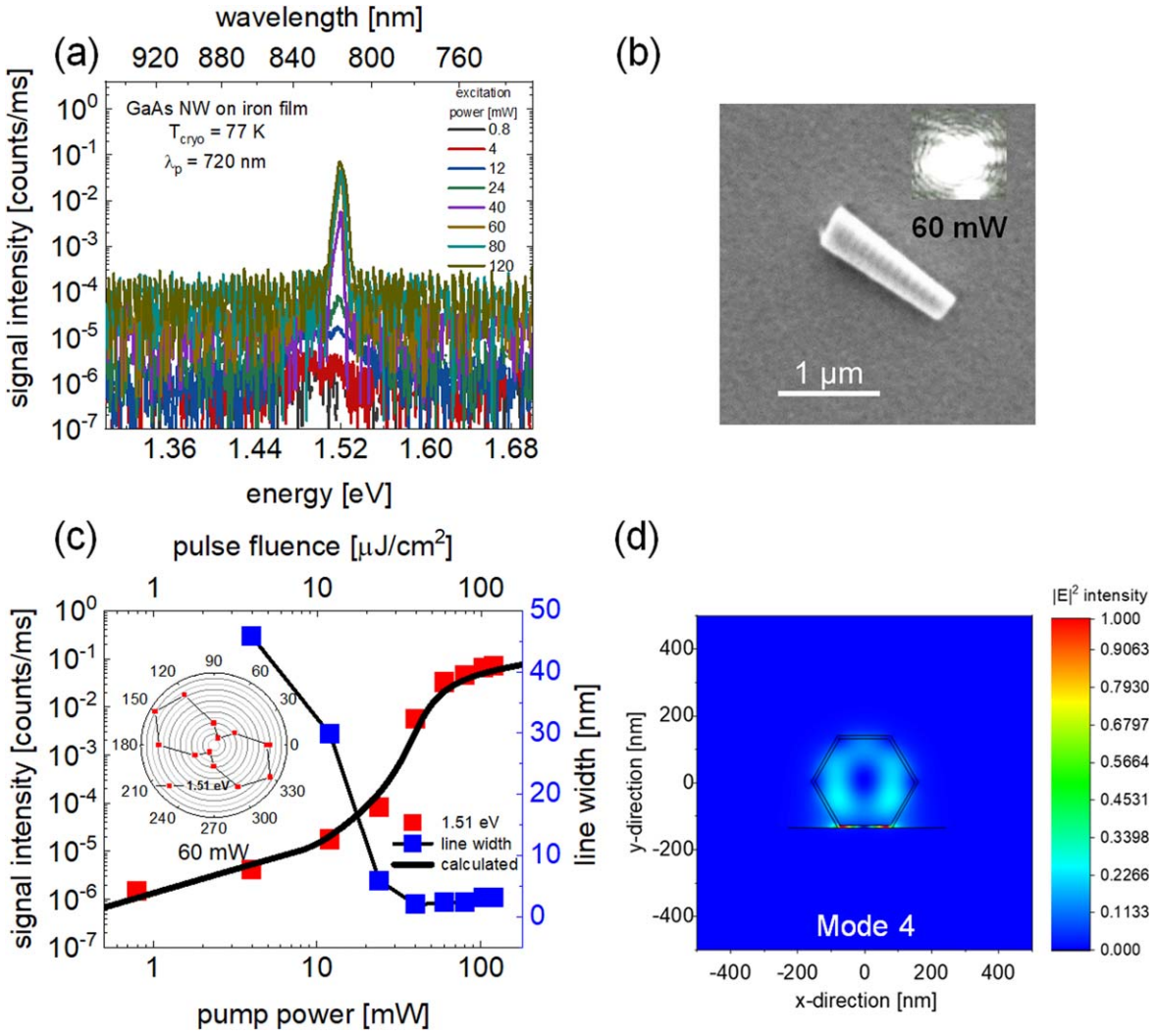

Figure 5. Single mode lasing from a short GaAs NW on iron film: (a) power dependent lasing spectra of a single GaAs NW at 77 K at an excitation wavelength of 720 nm. (b) SEM image of the lasing NW #8. The inset in (b) shows the interference pattern of the laser emission. (c) Peak intensity of the NW emission versus pump fluence obtained from lasing spectra in (a). The inset (c) shows the polar plot of the laser polarization. (d) Cross-sectional electric field profiles of the transverse lasing mode 4.

group indices for the waveguide modes were also theoretically calculated using FDTD modeling as described in [23] and shown in figure 3(c). The assignment of the transverse lasing modes (modes 1–6) to different NWs was performed by comparing the experimentally calculated group indices of the NWs with those calculated theoretically and displayed in figure 3(d). Most of the NWs have a group index n_g between 5 and 7. The NWs with tip diameters below 300 nm have an experimental group index similar to the calculated value of transverse mode 2 for NW #3 and NW #4 (see also table ST2 in the supplementary section). NWs with tip diameters between 325 and 375 nm (NW #2, #5, and #8) have an experimental group index close to the theoretical value of mode 4 (see table ST2 in the supplementary document). For NWs with a diameter greater than 375 nm (NW#1, NW#6, NW #7), mode 6 was the supported transverse laser mode, (see table ST2 in the supplementary document).

The mode assignment was further supported by calculating the threshold gain of individual NW lasers using equation (1) for different modes

$$\Gamma g_{\text{th}} = \alpha_p + \frac{1}{L}\ln\left(\frac{1}{R}\right) = \alpha_p + \alpha_R. \tag{1}$$

Here, Γ is the mode confinement factor, g_{th} is the threshold gain of the GaAs NW, L is the NW length, and R is the mode reflectivity at the end facets. α_p is the ohmic loss due to Fe film, calculated using the imaginary part κ of the effective index of the NW. The optical parameters for individual NWs were obtained from FDTD simulations (see figure 2). Modes with the least threshold value were deemed as the lasing mode for the respective NW. The values of the threshold and the assigned modes are shown in table ST2 of the supplementary document.

The lasing characteristics of the NWs on Fe film were studied by evaluating the laser output versus the laser pump power, i.e. *L–L* plot, using the coupled rate equation for the generated carrier and photon densities. The complete information and description of the equations and the modeling parameters are described in [23]. Figures 4(a), (d), and (g)

show experimentally obtained *L–L* plots from the power dependent measurements of NW #1, NW #5, and NW #3 on Fe film (refer to table ST1 and ST2) at 77 K. The inset in each *L–L* plot shows the optical image of the individual lasing NW, clearly showing an interference pattern due to lasing. The dimensions of the NWs were obtained from scanning electron microscopy (SEM) images, as shown in figures 4(b), (e), and (h) for NW #1, NW #5, and NW #3, respectively. The dimensions of these and other investigated NWs are listed in table ST1. The black lines in figures 4(a), (d), and (g) are the calculated *L–L* plots using the optical parameters obtained from the FDTD simulations and dimensions from SEM images. The threshold values obtained by fitting the calculated *L–L* curves with the experimental data were $g_{th} = 2400\,cm^{-1}$ (NW #1), $g_{th} = 3300\,cm^{-1}$ (NW #5), and $g_{th} = 4400\,cm^{-1}$ (NW #3), which are very close to the experimentally calculated threshold values of these NWs shown in table ST2. The calculated *L–L* plots are good fits to the experimental data and reproduce the threshold fluence for the lasing conditions of NW #1, #5, and #3 to be around ∼20–25 $\mu J\,cm^{-2}$. The variation in the threshold fluence of the different NWs is due to the disparity in the dimensions of the NWs and the values of their optical parameters. When the pump fluence reaches values above 60 $\mu J\,cm^{-2}$, the lasing intensity of the NWs starts to saturate, indicating the onset of Auger recombination as well as carrier induced transparency when the quasi-Fermi levels of exited holes and electrons reach the pumping photon energy of the pump laser.

The assigned transverse modes in NW #1, NW#5, and NW #3 are shown in figures 4(c), (f), and (i). Mode 6 in NW #1 with a tip diameter of 375 nm shows a nearly photonic mode which is predominantly confined within the NW. Mode 4 in the #NW 4 (tip diameter = 335 nm) shows a hybrid plasmonic-photonic mode, with a noticeable electric field confinement in the Al_2O_3 layer at the interface of the NW and the metal film. Mode 2 for NW #3 (tip diameter = 230 nm) also shows a weak electric field confinement in the Al_2O_3 coating. Examples of electric field profiles of different modes in GaAs NWs on Fe film with a tip diameter of 345 nm are displayed in figure S2 in the supplementary document.

Single mode lasing was observed at 77 K for NWs with a length smaller than 2 μm. Figure 5(a) shows pump power dependent 77 K lasing spectra of a short GaAs NW with a length of 1.45 μm, a tip diameter t_d of 300 nm, and a base diameter of 435 nm, as revealed in figure 5(b). The inset of figure 5(b) shows the interference pattern of the laser emission at a pump power of 60 $\mu J\,cm^{-2}$. Figure 5(c) depicts the laser peak intensity as a function of the exciting pump fluence. The fitted *L–L* curve for the NW is shown as a thick black line. An approximation like the one used for longer NWs was adopted to model the emission data of this short NW. The lowest calculated threshold gain value obtained from equation (1) was $4800\,cm^{-1}$ for the transverse hybrid photonic-plasmonic mode 4 (displayed in figure 5(d)). The inset of the *L–L* plot is the polarization-dependent measurement of the lasing mode. The linewidth versus intensity measurement in figure 5(c) shows a narrowing of the emission linewidth to ∼3 nm at a power greater than 80 $\mu J\,cm^{-2}$, indicating lasing condition.

Conclusion

Optically pumped lasing has been demonstrated in highly Zn-doped Al_2O_3/GaAs NWs on an Fe film at 77 K. Despite the metal loss, the NWs on Fe film show a moderately low threshold fluence of ∼20–25 $\mu J\,cm^{-2}$, for multimode and of ∼40 $\mu J\,cm^{-2}$ for single mode lasing. Lumerical simulations and *L–L* modeling suggest that lasing is preferably supported by the transverse modes 2, 4 or 6 depending on the tip dimension of the NW. Modes 2 and 6 show a weak plasmonic enhancement in the Al_2O_3 layer, whereas mode 4 corresponds to a hybrid photonic-plasmonic mode with a noticeable electric field confinement. Our investigation suggests that a ferromagnetic layer can be used to design and build magnetic field induced laser modulators with moderate plasmonic loss.

Acknowledgments

The authors acknowledge Dr M Fickenscher and Dr G Duscher for providing the SEM and TEM images and fruitful discussion. The Australian Research Council (ARC) is acknowledged for its financial support. The authors also acknowledge the use of the epitaxial facilities of the Australian National Fabrication Facility, ACT Node. Support from the National Science Foundation (NSF, grant DMR-2004768), the University Research Council (URC) at the University of Cincinnati and John Hauck Foundation at Xavier University are gratefully acknowledged.

Data availability statement

The data cannot be made publicly available upon publication because no suitable repository exists for hosting data in this field of study. The data that support the findings of this study are available upon reasonable request from the authors.

Disclosures

The authors disclose no conflict of interests.

Supplementary document

See the supplementary document for the results and discussion on material and film characterizations, nanowires dimensions, FDTD calculations of the optical properties of GaAs nanowires on iron film and electric field profiles.

ORCID iDs

Gyanan Aman https://orcid.org/0000-0002-4672-1829
Marc Cahay https://orcid.org/0000-0001-8087-5728
Hans Peter Wagner https://orcid.org/0000-0003-4347-1294

References

[1] Errando-Herranz C, Takabayashi A Y, Edinger P, Sattari H, Gylfason K B and Quack N 2020 MEMS for photonic integrated circuits *IEEE J. Sel. Top. Quantum Electron.* **26** 8200916

[2] Ma R M and Oulton R F 2019 Applications of nanolasers *Nat. Nanotechnol.* **14** 12–22

[3] Li C, Liu Z, Chen J, Gao Y, Li M L and Zhang Q 2019 Semiconductor nanowire plasmonic lasers *Nanophotonics* **8** 2091–110

[4] Couteau C, Larrue A, Wilhelm C and Soci C 2015 Nanowire lasers *Nanophotonics* **4** 90–107

[5] Gu Z Y, Song Q H and Xiao S M 2021 Nanowire waveguides and lasers: advances and opportunities in photonic circuits *Frontiers Chem.* **8** 613504

[6] Liang Y, Li C, Huang Y Z and Zhang Q 2020 Plasmonic nanolasers in on-chip light sources: prospects and challenges *Acs Nano* **14** 14375–90

[7] Sorger V J, Oulton R F, Ma R M and Zhang X 2012 Toward integrated plasmonic circuits *MRS Bull.* **37** 728–38

[8] Peng H T, Nahmias M A, de Lima T F, Tait A N, Shastri B J and Prucnal P R 2018 Neuromorphic photonic integrated circuits *IEEE J. Sel. Top. Quantum Electron.* **24** 6101715

[9] Vietmeyer F, Tchelidze T, Tsou V, Janko B and Kuno M 2012 Electric field-induced emission enhancement and modulation in individual CdSe nanowires *ACS Nano* **6** 9133–40

[10] Hurtado A *et al* 2013 Polarization switching in GaN nanowire lasers *Appl. Phys. Lett.* **103** 251107

[11] Li Q, Chen L, Xu H X, Liu Z W and Wei H 2019 Photothermal modulation of propagating surface plasmons on silver nanowires *ACS Photonics* **6** 2133–40

[12] Armelles G, Cebollada A, Garcia-Martin A and Gonzalez M U 2013 Magnetoplasmonics: combining magnetic and plasmonic functionalities *Adv. Opt. Mater.* **1** 10–35

[13] Sederberg S, Firby C J, Greig S R and Elezzabi A Y 2017 Integrated nanoplasmonic waveguides for magnetic, nonlinear, and strong-field devices *Nanophotonics* **6** 235–57

[14] Kalinowski J, Szmytkowski J D and Stampor W 2003 Magnetic hyperfine modulation of charge photo-generation in solid films of Alq(3) *Chem. Phys. Lett.* **378** 380–7

[15] Wang J L, Jiang H J, He Z, Liu J W, Wang R, Huang W R, Feng L T, Ren X F, Hou Z H and Yu S H 2020 Radial nanowire assemblies under rotating magnetic field enabled efficient charge separation *Nano Lett.* **20** 2763–9

[16] Ferreiro-Vila E, Garcia-Martin J M, Cebollada A, Armelles G and Gonzalez M U 2013 Magnetic modulation of surface plasmon modes in magnetoplasmonic metal-insulator-metal cavities *Opt. Express* **21** 4917–30

[17] Gabriel C J and Piller H 1967 Determination of optical verdet coefficient in semiconductors and insulators *Appl. Opt.* **6** 661

[18] Burgess T *et al* 2016 Doping-enhanced radiative efficiency enables lasing in unpassivated GaAs nanowires *Nat. Commun.* **7** 11927

[19] Valente J, Ou J Y, Plum E, Youngs I J and Zheludev N I 2015 A magneto-electro-optical effect in a plasmonic nanowire material *Nat. Commun.* **6** 7021

[20] Zayets V, Saito H, Ando K and Yuasa S 2012 Optical isolator utilizing surface plasmons *Materials* **5** 857–71

[21] Joyce H J *et al* 2011 III–V semiconductor nanowires for optoelectronic device applications *Prog. Quantum Electron.* **35** 23–75

[22] Kharmouche A and Bensehil I 2019 Synthesis, structural and magnetic properties of physical vapor deposited Fe/Si(100) and Fe/Si(111) thin films *J. Mater. Sci.-Mater. Electron.* **30** 631–8

[23] Aman G, Mohammadi F, Franzl M, Lysevych M, Tan H H, Jagadish C, Schmitzer H, Cahay M and Wagner H P 2021 Effect of Au substrate and coating on the lasing characteristics of GaAs nanowires *Sci. Rep.* **11** 21378

[24] Palik D 1998 *Handbook of Optical Constants* (New York: Academic)

[25] Weber J M 2002 *Handbook of Optical Materials* (Boca Raton, FL: CRC Press) Editor: CRC (https://doi.org/10.1201/9781315219615)